Evolutionary effects of rotation in massive stars and their circumstellar medium

B. Pérez-Rendón
Departamento de Investigación en Física, Universidad de Sonora,
Apartado Postal 5-088, Hermosillo, Sonora, México,
e-mail: brenda@cajeme.cifus.uson.mx

G. García-Segura
Instituto de Astronomía, Universidad Nacional Autónoma de México,
Apartado Postal 877, Ensenada 22800, Baja California, México,
e-mail: ggs@bufadora.astrosen.unam.mx

N. Langer
Astronomical Institute, Utrecht University,
P.O. Box 80000, 3508 TA Utrecht, The Netherlands,
e-mail: n.langer@uu.nl

Recibido el 29 de enero de 2008; aceptado el 19 de junio de 2008

Massive main sequence stars are fast rotators [1] but most of up to date evolutionary stellar models do not take account this important physical process. Stellar rotation affects the massive stellar evolution due to the rotationally induced mixing processes, the increase of mass loss rates, etc. [2] and stellar rotation also affects the circumstellar medium due to stellar wind interaction. The parameters of stellar wind depend on stellar luminosity, mass, radius and metallicity so the wind parameters change as the star evolves coupling the evolution of circumstellar medium to the star itself. In this work we used the stellar code STERN to investigate the evolution of a 29 $M_\odot$ massive star with solar composition including rotation and no-rotation with the same input physics, in order to study the effect of rotation in stellar evolution and their circumstellar medium. We observe that rotating star develops a Wolf-Rayet phase whereas the non-rotating star does not. We use the output of stellar code as inner boundary conditions in the hydrodynamical code ZEUS-3D to simulate the dynamical behavior of circumstellar medium around each star. As consequence of evolutionary changes induced by rotation the pre-supernova circumstellar medium is quite different for the same progenitor mass.

Keywords: Stellar rotation; stellar evolution; circumstellar medium.

Las estrellas masivas son rotadores rápidos [1]. Sin embargo, la mayoría de los modelos estelares recientes no toman en cuenta este importante proceso físico. La rotación estelar afecta la evolución de las estrellas masivas debido a los procesos de mezclado inducidos por rotación, al incremento en las tasas de pérdida de masa, etc. [2] a la vez que también impacta en el medio circunestelar debido la interacción del viento con el gas alrededor de la estrella. Los parámetros del viento estelar dependen de las características estelares como la luminosidad, masa, radio y metalicidad por lo que los parámetros del viento cambian conforme la estrella evoluciona, acoplando la evolución del medio circunestelar a la estrella misma. En este trabajo usamos el código estelar STERN para investigar la evolución de una estrella masiva de 29 $M_\odot$ con composición solar en dos modelos con las mismas características físicas excepto por la inclusión de rotación en uno de ellos, con el fin de estudiar el efecto de la rotación en la evolución estelar y el medio circunestelar. Observamos que la estrella en rotación desarrolla fase Wolf-Rayet mientras que la estrella sin rotación no. Usamos los datos de salida del código estelar como condiciones de frontera internas en el código hidrodinámico ZEUS-3D para simular el comportamiento dinámico del medio circunestelar alrededor de cada estrella. Observamos que como consecuencia de los cambios evolutivos inducidos por la rotación estelar el medio circunestelar pre-supernova es muy diferente para dos estrellas progenitoras de la misma masa inicial.

Descriptores: Rotación estelar; evolución estelar; medio circunestelar.

PACS: 97.10.Kc; 97.10.Cv; 97.10.Fy

1. Introduction

The effect of rotation on stellar models has received a special interest in recent years. Observational He and N excesses on OBA supergiants [3] and fast rotators [4] have revealed additional internal mixing in stars, beyond the achieved by simple convection and overshooting in non-rotation models. Rotationally induced mixing in stellar models produces surface enrichement of He and N [5, 6] able to reduce the differences between theory and observations. Rotation included in stellar models also has improved the understanding about other discrepancies between models and observations as the ratio of blue to red supergiants in galaxies, the blue Hertzpung gap, etc. [7].

Stellar rotation affects the massive stellar evolution due to the rotational mixing processes and the increase of mass loss rates [5]. This modifies the stellar wind parameters and thus the structure of the circumstellar medium at pre-supernova stage.

In this work we discuss the evolution of a 29 $M_\odot$ star and its circumstellar medium. Two sequences of stellar models are calculated with the same input physics except only in

the value of their initial rotational velocity in order to compare the effect of rotation in stellar and circumstellar medium evolution: we calculated a non-rotating model with an initial rotational velocity of $v_{rot} = 0$ km s^{-1} (model A) and a rotating model with $v_{rot} = 200$ km s^{-1} (model B).

2. Numerical methods

The numerical methods used in this work are similar to those in [8]. The stellar models have been produced with an one-dimensional (1D) implicit hydrodynamic code for stellar evolution "STERN" [9, 10] with solar metallicity (Y=0.28; Z=0.02). We use the Ledoux criterion for stellar convection, and the processes of convective transport are considered as diffusive processes according to [9]. Convective overshooting is formulated with the aid of the mixing length theory of convection, and it uses the mean path free of convective elements expressed by $L = \alpha_{over} H_p$, where H_p is the pressure scale height at the edge of the classical core and α_{over} is a free parameter. In our work convective overshooting was taken into account during core H-burning with an effective overshooting of α_{over} = 0.2. For convection we have adopted a mixing length parameter of $\alpha = \mathrm{L/H_P} = 1.0$ for the main sequence. On the red supergiant (RSG) phase the α parameter was set to 2.0, in order to avoid dynamical instabilities in the outer envelope related to high radiation pressure and partial ionization in the outer layers. In the calculations, we adopted the empirical formulation of the parametrical mass loss rate by [11]

$$\dot{M} = 9.63 \times 10^{-15} (L/L_\odot)^{1.24} (M/\mathrm{M}_\odot)^{0.16} \times (R/\mathrm{R}_\odot)^{0.81} \mathrm{M}_\odot \, /yr \qquad (1)$$

This mass loss rate is used for all the evolutionary stages, except in the RSG and Wolf-Rayet (WR) phases. On the RSG phase the Nieuwenhuijzen & de Jager mass loss rate [11] was enhanced multiplying it by a factor of 2.0.

The inclusion of rotation in model B modifies the hydrostatic equilibrium by adding a centrifugal acceleration term that modifies the momentum and energy transport equations in order to take into account this effect. The centrifugal forces lead to modify the shape of equipotential surfaces and therefore deviate the equations of spherical symmetry. For the rotational case the spherical mass shells correspond to equipotential surfaces of the effective potential ψ which includes gravity and centrifugal forces (in the conservative case). If V_ψ is the volume enclosed to the equipotential surface of the potential ψ, we use the equivalent radius r_ψ (defined as $r_\psi = (3V_\psi/4\pi)^{1/3}$) to write the stellar structure equations to keep the one dimensional treatment (details in Ref. 12). In this context, "STERN" takes account the stellar rotation following this approximation and the code was kept one dimensional. The centrifugal force is included according to the method described by Ref. 13 as has been described by Refs. 6 and 14. Stellar rotation also induces several instabilities causing mixing and changes the mass loss rate [15]. In STERN the rotationally induced mixing is included into models trough of several rotational instabilities as has been described in [6]. The enhancement on stellar mass loss rates is due to the effect of the centrifugal forces on the very outermost stellar layers. In this work we have used an enhanced mass loss rate according to [16], where the non-rotational mass loss rate is enhanced by the factor

$$\dot{\mathcal{M}}(\omega) \equiv \dot{\mathcal{M}}(\omega = 0) \times \left(\frac{1}{1-\Omega} \right)^{\varsigma}, \; \xi \approx 0.43 \qquad (2)$$

$\dot{\mathcal{M}}(\omega = 0)$ is the mass loss rate of the non-rotating star [Eq. (1)] and $\Omega \equiv v/v_{crit}$ is the ratio of the equatorial surface rotation rate to the critical rotation rate (break-up speed) defined by

$$v_{crit}^2 \equiv \frac{Gm}{r}(1-\Gamma), \qquad (3)$$

Here Γ is the Eddington factor.

From stellar models we have derived the mass loss rates and the terminal wind velocities as function of time and we have used them as time dependent, inner boundary conditions in the magnetohydrodynamical code ZEUS-3D, a three dimensional, finite-difference, eulerian explicit code [17]. We have computed the behavior of CSM in one dimension for main sequence and red supergiant phases and the post-RSG evolution was computed in two dimensional (2D) grid. The size of the computational 1D domain is $\mathrm{r_{max}} = 50\mathrm{pc}$, with 1,000 radial zones, giving spatial resolution of 0.05 pc/cell. Hereafter, in 29 $\mathrm{M}_\odot$ model the variables have been interpolated in a smaller 2D grid. The extent of two-dimensional grid was chosen to cover the entire modified medium around each stars. The computational 2D domain of model A was of r = 10 pc $\times \theta = 25°$, with 200×50 cells giving a resolution of 0.05pc $\times 0.5°$. In model B the computational 2D domain was r = 20 pc $\times \theta = 25°$, with 400×50 cells giving the same spatial resolution. We have not included wind anisotropies as function of stellar colatitude (aspherical winds).

3. Stellar evolution

3.1. Model A. Initial $\mathbf{V_{rot} = 0}$ km s^{-1}

Stellar evolution in model A was computed from ZAMS up to oxygen core exhaustion previous to Si burning to few days or hours from the SN explosion (pre-SN). Figure 1 shows the path followed by the model A in the HR diagram (HRD). The star evolves normally trough the main sequence (MS) during $\tau = 5.1$ Myrs and loses 1.53 $\mathrm{M}_\odot$ with an average mass loss rate of 2.8×10^{-7} $\mathrm{M}_\odot$ yr^{-1} by a fast wind ($\mathrm{v}_\infty \sim$ 1 000 - 3 000 km s^{-1}). After core H exhaustion the star becomes a RSG during 2.58 $\times 10^5$ and loses 17.1 $\mathrm{M}_\odot$. In the RSG stage, the stellar hydrogen envelope is enriched with He and N from the CNO in H shell burning. After RSG the star evolves to the blue side of the HRD to develope a blue loop as a Luminous Blue Supergiant (LBSG). During the blue loop, we have a new increase of He and N surface abundances.

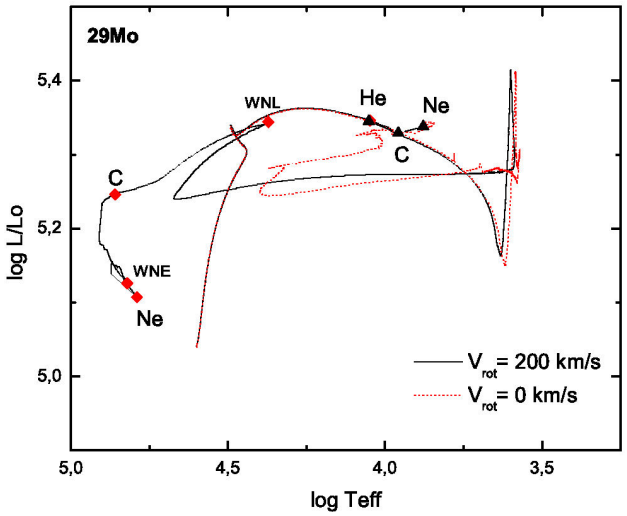

FIGURE 1. Evolutionary tracks for the 29 $M_\odot$ models (models A and B). Note that the stellar evolution is very similar up to the onset of the blue loop, thereafter the stellar track on HRD changes due to the difference in the mass loss rates. The filled triangles and rectangles mark the onset of the core burning phases in each model.

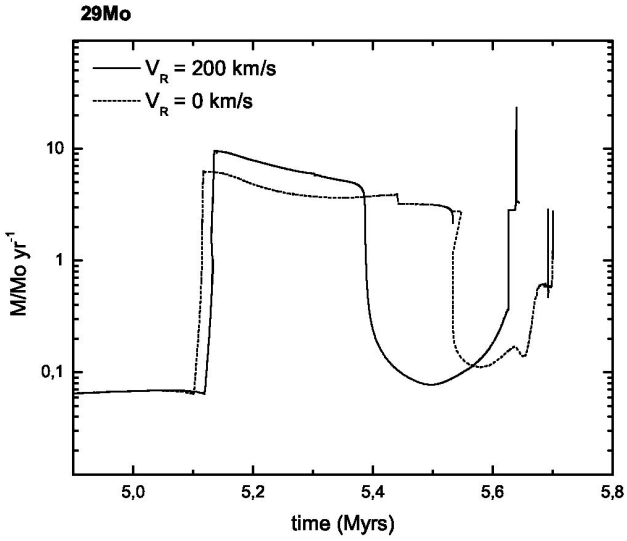

FIGURE 2. Comparison of mass loss rates of rotational case (model A) and non-rotational one (model B) on the RSG and post-RSG phases. On the RSG phase we use the Nieuwenhuijzen & de Jager mass loss rate [11] multiplied by a factor of 2.0. On WR stage (in model B) the rates are by Langer *et al.* (1989) [9]. Rotational mass loss rates are increased by the factor according to Eq. (2) in the text. In main sequence the mass loss rates are different only by 1% and the difference is enhanced from RSG onwards.

At 5.73 Myr, when He core mass fraction drops below $Y_c \sim 0.22$, the star goes back to the red side of the HRD. C core ignition occurs at 5.87 Myr followed by Ne and O burning. The beginning of each burning phase is pointed with filled rhombus in the HRD (Fig. 1). Note that from Ne core burning onwards, the location of the star in the HRD does not vary because of the short timescales of the late burning stages. The pre-SN model is an O core burning star with a final mass of $\sim 10 M_\odot$. The envelope has 0.34 $M_\odot$ composed mainly by H, He and N ($Y_s = 0.52$, $X_s = 0.46$, $N_{sup} = 0.008$). It has a $T_{\rm eff} \sim 7,509$ K and a $R_{\rm eff} \sim 277\ R_\odot$ and we tend to indentify it with a yellow supergiant (YSG) previous to the SN explosion. Using the envelope mass criterion from Heger *et al.* (2003) the explosion would be a SNIIb type. The evolutionary channel of this model is:

$$\mathrm{MS} \rightarrow \mathrm{RSG} \rightarrow \mathrm{LBSG} \rightarrow \mathrm{YSG} \rightarrow \mathrm{SNIIb}$$

3.2. Model B. Initial $V_{\rm rot} = 200$ km s^{-1}

Stellar evolution in model B was computed from ZAMS until core C exhaustion previous to core Ne burning. Figure 1 shows the evolutionary path in HRD of the model B in comparison with the non-rotational case. Duration of MS ($\tau = 5.113$ Myrs) in model B is slightly larger than non-rotational case because the rotating star is slightly less luminous due to the reduced effective gravity in the envelope [5]. The rotational internal mixing in MS is inhibited by gradients in the molecular weight [6] and in this stage the evolution of the rotating star is similar to non-rotational case. Rotational mass loss rate however is greater by a 1% in MS and the difference increases during RSG stage. The rotational velocity in ZAMS is 220 km s^{-1} and decreases to $\prec 10$ km s^{-1} in RSG due to the angular momentum conservation of the envelope in expansion. Mass loss rates of rotational and non-rotational case are shown in Figure 2. Rotating star has a shorter RSG phase than non-rotating star, but the mass loss rate is enhanced. At the end of RSG phase the stellar mass of rotating star is 10.2 $M_\odot$ versus 10.34 $M_\odot$ of the non-rotating star, so the stellar evolution is quite similar until the end of RSG stage as is shown in Fig. 1. Model B begins a blue loop extending into the main sequence band after the RSG stage. The blue loop of the rotating star is bluer than non-rotational model because the higher mass loss rate in RSG [18]. During the back to red side of HRD the high mass loss rate peels off the envelope and the H-surface drops below 40% ($X_s \prec 0.4$) so our rotating star becomes a Wolf-Rayet H-rich (WNL) star at 5.63 Myrs.

When the model B reaches a WR stage, the star evolves again to blue side of HRD. Unlike to another WR models, our rotating star has already exhausted the He in the core and it has a He burning shell surrounding the C/O core. At 5.633 Myrs our WNL star ignites C on the core. At the end of the core C-burning the star becomes a Wolf-Rayet H-poor (WNE). The central C-burning stage covers 5 700 yrs. After to C depletion in the core the STERN code develops numerical instabilities and stops. Our last model has an unburned O/Ne/Mg core with a temperature of 12 $\times 10^8$ K surrounded by a C burning shell. After core C depletion the rotationally induced mixing becomes unimportant [6] and the surface abundances remains "frozen", only changing due the stellar mass loss. The subsequent burning timescales are short how-

ever ($\sim 3 - 7 \times 10^2$ yrs) and the star will not lose a high amount of mass ($\prec 10^{-3} M_\odot$). The evolutionary channel of model B is then:

$$\mathrm{MS} \rightarrow \mathrm{RSG} \rightarrow \mathrm{LBSG} \rightarrow \mathrm{WNL} \rightarrow \mathrm{WNE} \rightarrow ?? \rightarrow \mathrm{SN?}$$

4. Hydrodynamical simulations

The numerical methods used in hydrodynamical calculations are similar to those in [19], [8]. We do not consider the effects of photoionization from stellar radiation, magnetic fields nor heat conduction. For simplicity, the numerical calculation are divided into three stages: MS (1D), RSG (1D) and blue loop or WR star (2D). Our hydrodynamical calculations start at ZAMS, in a homogeneous and quiescent ambient medium with an uniform density of $n_o = 13 \mathrm{cm}^{-3}$ and an initial thermal energy density of $1 \times 10^{-13} \mathrm{erg/cm}^3$.

Figure 2 shows the mass loss rates as a function of time obtained from the stellar evolution calculations. First, during the MS stage the mass loss rate slightly increases whereas the star wind velocity drops. During this stage the wind kinetic energy is converted into thermal energy by collision at the reverse shock, forming an adiabatic bubble surrounded by a shocked, swept-up shell of interstellar material (MS shell) [20].

For the second stage (RSG) the mass loss rate increases nearly by two order of magnitude and the RSG wind is much slower and denser than MS wind. We have performed the CSM evolution for RSG phase in 1D, since the RSG shell is quite stable for low RSG wind velocities [19]. Faster winds are subject to Rayleigh-Taylor (RT) instability (for LBVs see Ref. 21; for RSG see Ref. 22). The RT instability produces fingers in the RSG shells, but the instability does not affect the position of their inner edge.

The duration of the RSG stage is different for each star but the impact on the CSM is quite similar. During RSG, the winds build up shocked shells where the ram pressure of the RSG wind balances the thermal pressure of the main sequence bubbles. The larger RSG shell corresponds to model A since non-rotating model spends a longer time as RSG (Fig. 2). Position of RSG shells at the end of RSG phase are shown in Figs. 3 and 4 at slice 1 in clockwise from left.

In general the hydrodynamical evolution of both models is quite similar except from the end of RSG onwards. On the third stage the model A evolves to blue side of HRD performing a blue loop. The wind velocity increases to reach a maximum value of 550 km s^{-1} according to empirical LBSG wind velocities. The interaction of the supersonic LBSG wind with the slow and dense RSG wind material produces a double shock front stucture, and a new bubble of hot shocked wind (*LBSG bubble*). The thermal pressure of the bubble pushes the medium in an quasi-adiabatic shock and set up a new shell of shocked, swept-up RSG wind (*LBSG shell*). Figure 3 shows the formation of the LBSG shell through the blue loop. The LBSG shell is affected by RT instabilities at the interface, when it is accelerated by the LBSG bubble pressure.

The expansion velocity of the LBSG shell (35 km s^{-1}) is higher than the one of RSG shell (5 km s^{-1}), and the LBSG and RSG shells remain separated for $\sim 10^5$ yr until their collision. The collision between both shells is shown in Figure 3 in slice 5. The peak density of the LBSG shell is 2.6 times larger than the RSG shell. Both shells merge to form a massive shell (LBSG+RSG shell) moving out with a common velocity of ~ 18 km s^{-1} into the MS bubble. The massive shell develops RT instabilities in the outer edge, since the shell is decelerating. The outer edge is subsonic with respect to the MS bubble, and there is not a forward shock.

The final position of the dense shell is 6.0 $\pm$ 0.2 pc. It has a swept-up mass of 16.6 $M_\odot$ and a peak density of $\rho \sim 6.5 \times 10^{-24} \mathrm{gr/cm}^3$. The mass of the wind inside the LBSG bubble is smaller than 0.05 $M_\odot$. The density profile

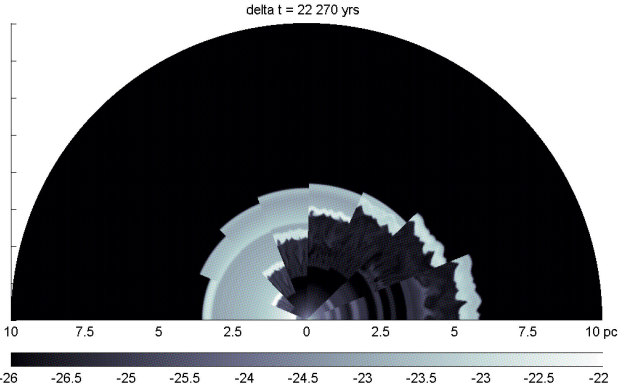

FIGURE 3. Post-RSG evolution of the circumstellar medium in model A. The figure shows the logarithm of gas density (g cm^{-3}). The CSM at the onset of LBSG phase (t = 5.544×10^6 yr) is shown on the left slice. The evolution runs clockwise. Slices have a Δt = 22 270 yr. Slice 8 occurs at t = 5.700×10^6 yr, when the star is at core O exhaustion (pre-SN).

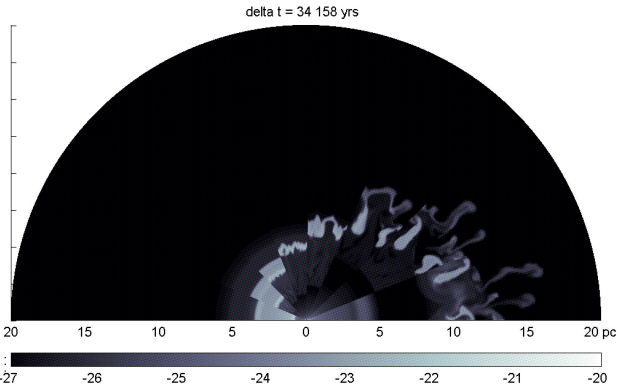

FIGURE 4. Post-RSG evolution of the circumstellar medium in model B. The figure shows the logarithm of gas density (g cm^{-3}). The CSM at the onset of LBSG phase (t = 5.405×10^6 yr) is shown on the left slice. The evolution runs clockwise. Slices have a Δt = 34 148 yr. Slice 8 occurs at t = 5.644×10^6 yr, when the star has a O/Ne/Mg core previous to Ne core ignition almost in pre-supernova.

of the pre-SN medium around the star of 29 $M_\odot$ (model A) is shown in slice 8 of Figure 3. The LBSG shell is composed mainly by H, He and N because it was formed from swept-up RSG wind. The LBSG wind is enhanced with He and N, and it is H deficient, although H still is an important wind component. The stellar surface of the pre-supernova LBSG is He, H and N abundant in that order.

Circumstellar evolution of model B differs from the non-rotational case. After the RSG phase model B also develops a blue loop phase, but during the back to red evolution sheds their H envelope and it becomes a WR star with faster wind ($\succ$ 1 000 km s^{-1}) and with lower density than the RSG wind. At the onset of the WR phase the RSG shell is located at 3.1 pc (slice 1, Fig. 4). It is ionized by the intense stellar radiation coming from the WR star and it temperature increases to the photoionization equilibrium temperature (T $\sim 10^4$ K). The wind velocity increases during LBSG and the interaction of the supersonic LBSG wind with the RSG wind produces a *LBSG bubble* that drifts away. The mechanical luminosity of wind is higher due to the high mass loss rate and the LBSG shell is faster than in model A case. The collision between LBSG and RSG shells is shown in Fig. 4, slice 4. Both shells merge to form a massive shell moving out with a common velocity of $\sim$ 30 km s^{-1} . RT instabilities appears at the outer edge of the shell and grow until breaking the shell to form several clumps and tails of dragged shell material. The clumps are slowly accelerated by the expansion of the subsonic shocked LBSG wind. At the end of the blue loop the model B becomes a WR and the mechanical luminosity of wind increases shifting away the inner edge of LBSG bubble. Finally, free wind of WR collides directly with the clumps that now are accelerated by this supersonic free wind. Bow shocks appears around to densest clumps. Figure 4 shows the logarithm of gas density at the end of the RSG phase (slice 1), the formation of the LBSG shell (slices 2,3), collision and breakout (slices 4,5,6) and the increase of mechanical luminosity due to WR wind (slice 8). The expansion velocity of the broken shell is $\sim$ 100 km s^{-1} . At the end of the stellar life, the fragmented shell consists in dense knots lying at a distance greater than $\sim$ 10 pc and irregular tails that are spread in an annulus of 10 pc of inner boundary and $\sim$ 15 pc in the outer edge (the MS shell is $\sim$ 35 pc).

5. Summary and conclusions

Rotationally induced mixing and the enhanced mass loss rates changes the stellar evolution for stars with the same initial mass and metallicity as has been shown in this work for a 29 $M_\odot$ star. The evolution of a star depends on initial mass, metallicity *and* rotation rate. The evolution of circumstellar medium is tightly bound to stellar evolution so the rotational effects also affect the circumstellar gas. This effect acquires a special importance in massive stars because the supernova blast wave will interact with the modified medium. In our 29 $M_\odot$ models the stellar evolution was different and each star build up different pre-supernova media. The pre-supernova medium around our non-rotating star (model A) is a dense and massive shell at 6.3 pc from the central star, formed after the collision of the LBSG shell with the previous RSG shell. Rotating star (model B) also produces a LBSG shell that collides with the RSG shell to form high density clumps moving outward into the MS hot bubble, covering a distance from 10-15 pc. The distribution of density, temperature, chemical composition and velocity field of the pre-supernova circumstellar medium are different in both cases, for the same initial mass. This difference affects the dynamics of supernova blast wave. We have confirmed that the initial rotation rate is a fundamental parameter for structure and evolution of massive stars and their circumstellar media. The inclusion of stellar rotation in new stellar models is a mandatory task for future studies.

Acknowledgements

We would like to thank our anonymous referee for his valuable comments, which have benefited this manuscript. We also thank Michael L. Norman and the Laboratory for Computational Astrophysics for the use of ZEUS-3D. BPR also acknowledges support by CONACYT Retención fellowship.

1. I. Fukuda, *PASP* **94** (1982) 271.
2. A. Heger and N. Langer, *ApJ* **544** (2000) 1016.
3. K.A. Venn, D.L. Lambert, and M. Lemke, *A&A* **307** (1996) 849.
4. A. Herrero *et al.*, *A&A* **261** (1992) 209.
5. A. Maeder & G. Meynet, *ARA&A* **38** (2000) 143.
6. A. Heger, N. Langer, and S.E. Woosley, *ApJ* **528** (2000) 368.
7. G. Meynet & A. Maeder, *A&A* **321** (1997) 465.
8. B. Pérez-Rendón, G. García-Segura, and N. Langer, submitted to *A& A*.
9. N. Langer, M.F. El Eid, and K.J. Fricke, *A& A* **145** (1985) 179.
10. A. Heger, PhD Thesis. Technische Universität München (1998).
11. H. Nieuwenhuijzen, C. de Jager, *A & A* **231** (1990) 134.
12. A.S. Endal & S. Sofia, *ApJ* **210** (1976) 184.
13. R. Kippenhahn & H.-C. Thomas, in IAU Colloq. 4, Stellar Rotation, ed. A. Slettebak (Dordrecht: Reidel) (1970) 20.
14. J. Fliegner, diploma thesis, Univ. Sternw. Gottingen (1993).
15. G. Meynet, lectures, CNRS school, will be published by Springer; arXiv:0801.2944v1 [astro-ph] (2008).
16. D.B. Friend & D.C. Abbott, *ApJ* **311** (1986) 701.

17. J.M. Stone and M.L. Norman, *ApJS* **80** (1992) 753.

18. B. Salasnich, A. Bressan, and C. Chiosi, *A&A* **342** (1999) 131.

19. G. García-Segura, N. Langer, and M.M. Mac Low, *A& A* **316** (1996) 133; paper A.

20. T.A. Weaver, R. McCray, J. Castor, P. Shapiro, and R. Moore, *ApJ* **218** (1977) 377.

21. G. García-Segura, M.M. Mac Low, and N. Langer, *A& A* **316** (1996) 133; paper B.

22. V. Dwarkadas, *ApJ* **667** (2007) 226.